UPCommons

Portal del coneixement obert de la UPC

http://upcommons.upc.edu/e-prints

Numerical study of heat transfer from a synthetic impinging jet with a detailed model of the actuator membrane

A. Miró[a, b], M. Soria[a,] , J.C. Cajas[b], I. Rodríguez[a]

[a] *Turbulence and Aerodynamics in Mechanical and Aerospace Engineering, Research Group (TUAREG), Universitat Politècnica de Catalunya (UPC), 08222, Spain*
[b] *Barcelona Supercomputing Center, 08034, Barcelona, Spain*

ARTICLE INFO

ABSTRACT

Synthetic jets are produced by the oscillatory movement of a membrane inside a cavity, causing the fluid to enter and leave through a small orifice. The present study is focused on investigating the cooling capabilities of a synthetic jet enclosed between two parallel isothermal plates with an imposed temperature difference. The unsteady three-dimensional Navier-Stokes equations have been solved for a range of Reynolds numbers from 50 to 1000 using time-accurate numerical simulations. A detailed model based on an Arbitrary Lagrangian-Eulerian (ALE) formulation is used to account for the movement of the actuator membrane. All the resulting flows are inherently three-dimensional and dominated by two major vortices, which find their counterparts inside the actuator cavity. A new structure, which is not found in open cavities, appears as an interaction of the synthetic jet flow with the bottom wall and results in a change on the jet's heat transfer mechanisms. Analysis of the outlet temperature has shown that assuming a uniform profile is reasonable if the Reynolds number is high enough, however, the outlet jet temperature is significantly higher than the cold plate temperature. Finally, this study proposes correlations for the heat transfer at the hot wall and the outlet temperature with the Reynolds number, which can be used to account for the cavity effects without the computationally expensive ALE model.

1. Introduction

Synthetic Jet (or Zero Net Mass Flow) Actuators [1 6] (SJAs) consist of a cavity with a mechanically moving diaphragm. Its actuation changes the cavity volume periodically, causing external fluid to enter and leave through a small slot. Under certain conditions, the advected vortices are too far to be ingested back. If so, a train of vortices (and eventually a jet) are created without the addition of mass flow, allowing the transfer of kinetic energy and momentum to a fluid medium without the need of piping systems.

Smith and Glezer [6] investigated the formation and evolution of SJAs. They defined the concept of stroke length and proposed a SJA characteristic velocity based on this definition. It was found out that the evolution of the SJA flow near the orifice is dominated by its time-periodic formation and advection of vortex pairs that roll up and become part of the jet. These vortices eventually become turbulent and lose coherence. It was also observed that their mean trajectory scales with the stroke length. On a later stage, Utturkar et al. [7] and Holman

et al. [8]. proposed a jet formation criteria (JFC) that has to be greater than a constant K that depends on geometric factors.

The flow patterns resulting from the interaction of the currents entering and leaving the cavity are very complex and have been the subject of many numerical and experimental studies. To mention just a few: Kral and Donovan [2] performed early studies on an incompressible laminar and turbulent two-dimensional synthetic jet using a URANS model (Spalart-Allmaras). They realized the importance of selecting an adequate boundary condition to simulate an isolated SJA and succeeded in implementing the orifice as a suction/blowing boundary condition. Their simulations presented a good correlation with that of Smith and Glezer. Kotapati et al. [9] performed span-wise periodic direct numerical simulations (DNS) of a synthetic jet previously analyzed with particle image velocimetry (PIV) by Yao et al. [10]. in the framework of the NASA LaRC Workshop, 2004. Despite simplifying the actuator geometry, it was found out that the results closely agree with the experimental results. Secondary structures surrounding primary vortices were found to cause transition to turbulence at a short distance from the orifice. In addition, large time scales were found and a sampling time of the order of 100 cycles was estimated to be required to

obtain accurate statistics for the external flow. Due to the aforementioned vortical nature of the SJA flow, the analysis of the vortices becomes a key parameter for the understanding of the flow dynamics. Silva-Llanca et al. [11]. compared different techniques for identifying coherent structures in synthetic jets and selected the Q-criterion [12] as a vortex presence indicator.

Synthetic jet impingement is of interest in heat transfer and has been the subject of many studies [13 17]. In particular, Silva-Llanca et al. [11,18]. performed several investigations on SJAs, both experimental and numerical. Experimental investigations were performed on two-dimensional impinging synthetic jets, managing to decouple the effects of Reynolds and Stokes numbers, thus varying independently the jet velocity and the jet driving frequency aiming for a better understanding of the jet dynamics. Good correlation was obtained between experimental and numerical results (using a simplified actuator model). They investigated the impingement phenomena for different aspect ratios and found out that for a jet-to-surface spacing of 5 could be optimal for their SJA configuration. As for jet-to-surface spacings greater than 5, the merging of consecutive vortex pairs occurs prior to the impingement and diminishes the overall heat transfer. Later [11], a canonical geometry was proposed in order to investigate the flow of a purely oscillatory jet, where a new formulation for the jet characteristic velocity was introduced. They observed that vortex coalescence reduces the heat transfer capacity of the jet and that secondary vortices with opposite circulation are generated when the vortex pair arrived near the heated wall. This was in good agreement with Ghaffari et al. [19], who experimentally investigated different jet-to-surface spacings using the PIV technique. It was found that the optimal ratio of jet-to-surface spacing that maximizes heat transfer is between 5 and 10.

SJAs have been proposed for cooling of circuit boards and miniature electronics [19,20], among other applications. These studies consider an open configuration in which the synthetic jet impinges to a hot wall using a simplified actuator model, as the heated flow is not ingested back inside the actuator and the temperature at the SJA outlet can be assumed constant [21 23]. The present study, however, is devoted to a configuration where the jet is enclosed between two parallel plates. Experimental investigations of this configuration were performed by Vukasinovic and Glezer [24] on an axisymmetric synthetic jet. It was found that the temperature of the jet at the expulsion is significantly above the ambient temperature due to a countercurrent in the flow formed by the confining plate. Moreover, the cooling efficiency of the jet was observed to decrease with the spacing between the parallel plates. Very recent numerical studies of opened and enclosed configurations of an axisymmetric synthetic jet, using moving mesh techniques for the membrane description, have been performed by Hatami et al. [25]. Noticeable differences were found in the flow and heat transfer capabilities between the enclosed and opened configurations. In particular, the advected vortices were found to stretch axially on the enclosed configuration whereas in the opened configuration they stretch radially. This has been found to produce more coherent vortices in the opened configuration compared with the enclosed configuration. As aforementioned, under these circumstances, the external flow interacts with the flow inside the SJA cavity as is ingested back inside the actuator, thus making the conditions at the actuator outlet hard to estimate. Therefore, a formulation that imposes the movement of the membrane position through Arbitrary Lagrangian-Eulerian (ALE) formulation is proposed to describe a canonical synthetic jet actuator geometry. ALE formulation has been successfully used to model the time-dependent movement of the SJA membrane [26]. Other implementations in the literature for realistic models of the SJA membrane are Chimera grids [27], virtual forces to emulate the effect of a moving boundary [28], the mass-spring analogy method [29], and dynamic mesh methods [25]. ALE allows imposing physically realistic boundary conditions for the momentum and energy equations at the actuator membrane. The other closures that exist in the literature, for example, imposing an inlet velocity [9] or the velocity at the SJA outlet [18,22], would not be suitable for the present configuration. In addition, the present study also devotes to understand the impact of the turbulence inside the cavity to the external flow and the impingement.

The objectives of this paper are threefold: (i) Firstly, to provide a better understanding of the SJ flow enclosed between two parallel plates for the range of Reynolds numbers from 50 to 1000 by studying the vortices formed in the external and internal flow. (ii) Secondly, to present a formulation and to provide a detailed model of the SJA membrane movement using ALE techniques that allow to study the flow and heat transfer mechanism inside the actuator cavity, aiming to provide a better approximation of the flow and temperature at the SJA neck. (iii) Thirdly, to provide a correlation of the Nusselt number and the averaged outlet temperature with the Reynolds number for a given jet-to-surface spacing of 5 and JFC = 3, as well as velocity and temperature profiles at the actuator outlet for the Reynolds numbers studied.

This paper is structured as follows: Firstly, the geometry of the case is defined in detail. Then, the mathematical and numerical models are discussed, highlighting the formulation used for the membrane movement and performing a domain and grid sensitivity analysis. Afterwards, the results are examined, starting by a study of the instantaneous flow evolution and an analysis of its temporal spectrum to find which are the dominant frequencies of the flow. This is followed by an investigation on the time and phase averaged flow to show the main structures of the flow, as well as the velocity and temperature profiles at the actuator outlet. Finally, the discussion closes with an inspection on the jet heat transfer at the hot wall.

2. Definition of the case and mathematical model

A simplified rectangular actuator in an homogeneous domain in the x_3 direction as in Fig. 1 is considered. The domain is wide enough ($L/d = 60$) so as not to interfere with the development of the jet. The jet impinges on an uniformly heated wall located at a jet-to-surface distance $H/d = 5$, imposed according to the optimal distances for cooling applications [13,18,19], and causes convective heat transfer from the wall to the jet. A depth of $D/d = 6$ is considered to allow the full development of the three-dimensional flow, as reported in Ref. [9]. This is further confirmed by the autocorrelations presented in Section 2.2. The dimensionless actuator cavity width W/d is set to impose a certain jet formation criteria (JFC = 3), as later discussed. The other dimensions of the SJA are selected as in Liu [30], with $b/d = 0.3$ and $B/d = 1.67$.

The Navier-Stokes and energy equations are used to model the flow. Incompressible regime is assumed as the ratio of the Helmholtz frequency of the actuator and the drive frequency assumed to be less than 0.5 [31,32]. The present study focuses on situations where the jet velocity is high enough to disregard natural convection, i.e., the Richardson (Ri) number, defined as the ratio of the buoyancy term to the flow shear term, is low enough. Experimental and numerical studies [23] show that buoyancy effects become relevant for Richardson $Ri > 0.01$. Also, for the present work, thermal radiation is neglected. Under these hypotheses, the incompressible Navier-Stokes equations are

$$\frac{\partial u_j}{\partial x_j} = 0 \tag{1}$$

$$\rho \frac{\partial u_i}{\partial t} + \rho \frac{\partial \left(u_i u_j \right)}{\partial x_j} = -\frac{\partial p}{\partial x_i} + \frac{\partial}{\partial x_j} \left[\mu \left(\frac{\partial u_i}{\partial x_j} + \frac{\partial u_j}{\partial x_i} \right) \right] \tag{2}$$
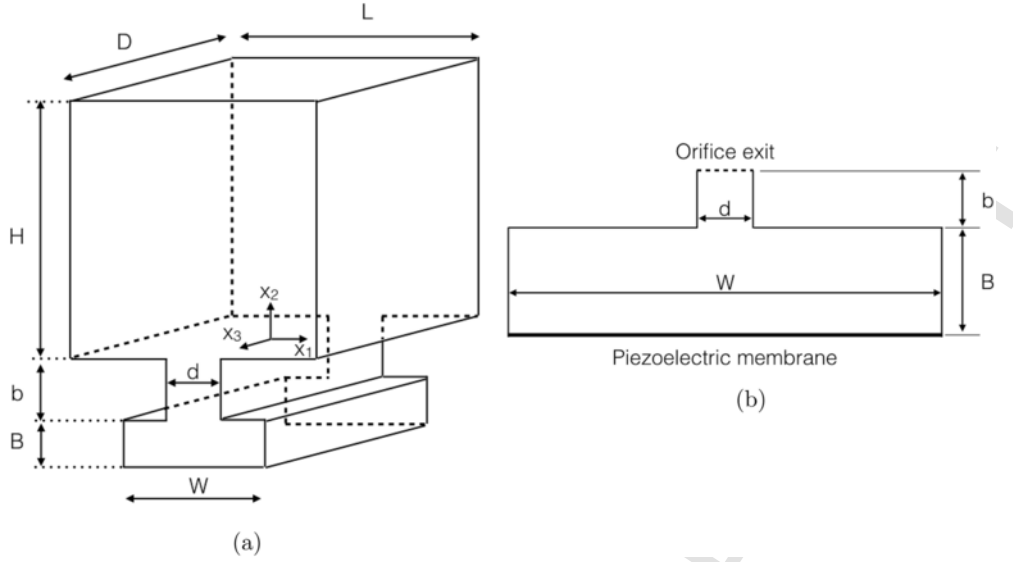
Fig. 1. Studied configuration geometry (not to scale). (a) Schematic view of the whole domain. (b) Detail of the actuator geometry.

$$\rho c_p \frac{\partial T}{\partial t} + \rho c_p \frac{\partial (u_j T)}{\partial x_j} = \frac{\partial}{\partial x_j}\left(k\frac{\partial T}{\partial x_j}\right) \tag{3}$$

where x_i are the spatial coordinates (or x, y and z), u_i are the cross-stream, stream-wise and span-wise velocity components (or u, v, w), p is the pressure and T is the temperature. is the density, is the dynamic viscosity, c_p is the specific heat coefficient at constant pressure and k is the thermal conductivity of the fluid.

The Reynolds number is defined along the standard set by Smith and Glezer [6] as

$$Re = \frac{\rho U_0 d}{\mu} \tag{4}$$

where d is the orifice diameter (see Fig. 1) and U_0 is a characteristic velocity defined in terms of the stroke length L_0 as $U_0 = L_0 f_0$, and f_0 is the SJA membrane oscillating frequency. In turn, the stroke length is defined as

$$L_0 = \frac{1}{d}\int_0^{\tau/2}\int_{-d/2}^{d/2} u_2 dx_1\, dt \tag{5}$$

where u_2 is the instantaneous dimensional vertical velocity at the orifice ($x_2 = 0$) and is the period. The Prandtl number is $Pr = (\ c_p)/k$ and takes an assumed value of 0.71, whereas the Strouhal number Sr is

$$Sr = \frac{2\pi f_0 d}{U_0} \tag{6}$$

As an alternative to the Strouhal number, some authors [7,9,18] define the Stokes number as

$$Sk = \sqrt{\frac{\rho 2\pi f_0 d^2}{\mu}} \tag{7}$$

that can also be used to characterize the flow.

The relationship between Reynolds, Strouhal and Stokes numbers is given by the jet formation criteria (JFC) [7,8], which is defined as

$$\text{JFC} = \frac{1}{Sr_{\bar U}} = \frac{Re_{\bar U}}{Sk^2_{\bar U}} \tag{8}$$

and is based on a time and space averaged velocity $\bar U$ at the SJA exit during the expulsion stroke ($\bar U = 2U_0$). For the span-wise periodic rectangular jets considered in the present work, if the JFC is lower than an approximated value of 2 [8], the jet is not formed.

In the present work, rather than imposing a velocity at the SJA neck as a boundary condition, the membrane position is modeled as

$$x_2 = -\delta(x_1)\cos(2\pi f_0 t) \tag{9}$$

where (x_1) is a shape function. A mean amplitude can be defined as

$$\bar A = \frac{1}{W}\int_{-W/2}^{W/2}\delta(x_1)\,dx_1 \tag{10}$$

where W is the actuator cavity width (see Fig. 1). Then, the characteristic velocity U_0 can be related to the mean amplitude and the drive frequency $U_0 = 2\bar A f_0 W/d$, thus coupling f_0 and U_0. Also, under this definition, the jet formation criteria becomes a purely geometrical parameter.

$$\text{JFC} = \frac{2}{\pi}\left(\frac{\bar A}{d}\right)\left(\frac{W}{d}\right) \tag{11}$$

Therefore, as seen by Smith and Glezer [6], when the motion of the actuator membrane is time-harmonic the formation parameters of the jet depend only on the amplitude of the actuator, and cannot be varied independently. High amplitudes and large jet cavity aspect ratios favor the formation of jets, independently of the frequency, while changing the drive frequency has no effect on the JFC. The present work is based on keeping JFC at a constant value of JFC = 3 and focusing the study on the effects of the Reynolds number.

2.1. Numerical model

The Reynolds numbers considered are $Re = 50$, 100, 300, 500, and 1,000. For $Re = 50$, 100, DNS are performed, whereas, for $Re > 100$, simulations are carried out using Large-Eddy Simulations and the filtered equations are used instead

$$\frac{\partial \widetilde{u}_j}{\partial x_j} = 0 \tag{12}$$

$$\rho \frac{\partial \widetilde{u}_i}{\partial t} + \rho \frac{\partial \left(\widetilde{u}_i \widetilde{u}_j \right)}{\partial x_j} = -\frac{\partial \widetilde{p}}{\partial x_i} + \frac{\partial}{\partial x_j} \left[\mu \left(\frac{\partial \widetilde{u}_i}{\partial x_j} + \frac{\partial \widetilde{u}_j}{\partial x_i} \right) \right]$$
$$- \frac{\partial \mathscr{T}_{ij}}{\partial x_j}$$

(13)

$$\rho c_p \frac{\partial \widetilde{T}}{\partial t} + \rho c_p \frac{\partial \left(\widetilde{u}_j \widetilde{T} \right)}{\partial x_j} = \frac{\partial}{\partial x_j} \left(k \frac{\partial \widetilde{T}}{\partial x_j} \right) - \frac{\partial \mathscr{Q}_i}{\partial x_j}$$

(14)

where $\widetilde{}$ denotes the filtered magnitudes. Eqs. (13) and (14) include the sub-grid scale (SGS) stress tensor $\mathscr{T}_{ij}$ and scalar flux $\mathscr{Q}_i$ that must be modeled. The present paper uses the wall-adapting local eddy viscosity model (WALE) [33] to close the formulation for the SGS stress tensor. This model is formulated in a way that it is suitable for unstructured grids and has the property of not acting near the walls or in two-dimensional flows. Moreover, its dissipation is relatively small in transitional flows. Regarding the SGS scalar flux, a gradient diffusion approach [34] is used. A fractional step approach is selected to solve the pressure-velocity coupling. The set of equations is time-integrated using an energy-conserving fourth-order Runge-Kutta explicit method [35]. With this approach, numerical stability imposes a maximum time-step that is estimated as described in Ref. [36]. In order to simplify the notation, when discussing the results the symbol $\widetilde{}$ will be dropped if $Re > 100$. Moreover, the results will be expressed in dimensionless form where $\widehat{x}_i = x_i/d$ is the dimensionless spatial coordinates, $\widehat{u}_i = u_i/U_0$ the dimensionless velocity components and $\widehat{T} = \left(T - T_\infty \right) / \left(T_{wall} - T_\infty \right)$ the dimensionless temperature and T_{wall} denotes the temperature at the heated wall and T_∞ the bulk temperature.

Non-slip boundary conditions are imposed at the top ($\widehat{x}_2 = H/d$) and bottom ($\widehat{x}_2 = 0$) of the discharge cavity as well as at the actuator walls including the SJA actuator membrane ($\widehat{x}_2 < 0$). Free-flow boundary conditions are prescribed at all the vertical boundaries with $\widehat{x}_2 > 0$. Regarding the energy equation, the cavity top wall is hot ($\widehat{T} = 1$) and the bottom wall is cold ($\widehat{T} = 0$). The lateral boundaries are considered adiabatic ($\partial \widehat{T}/\partial n = 0$). The SJA walls ($\widehat{x}_2 < 0$) are assumed to be cold. Periodic boundary conditions are set between the front ($\widehat{x}_3 = 0$) and back ($\widehat{x}_3 = D/d$) faces. The SJA membrane movement has been modeled using Eq. (9) and using ALE methods [37].

Statistically accurate representations of the flow are needed in order to understand the SJA flow. However, the overall system contains very slow temporal scales related with the low velocity zones, despite the intense mixing in the jet vicinity. This results in a very large computational time for the flow to reach statistical stationary conditions.

vFor this reason, precursory two-dimensional laminar (for $Re = 50, 100$) and URANS (for $Re > 100$) simulations using the k ω SST [38] model with a large time-step have been analyzed to estimate the time scales associated with the process. Fig. 2 (a) shows the temporal evolution of the temperature at maximum expulsion ($t = 0$) and maximum ingestion ($t = \tau/2$) for one precursory simulation at $Re = 500$ and reveals that about 100 actuator cycles are needed to reach stationary conditions. Therefore, the flow has been initialized using these precursory simulations in order to reduce the computational time. With this strategy the statistical stationary state is reached with about 50 actuator cycles,v as can be seen in Fig. 2 (b).

Moreover, the initial conditions for the finer meshes are generated from the solution obtained with coarser grids, which in turn reduced the initial transient by 20 cycles. Once the statistical stationary state is reached, the simulations are run for 30 actuator cycles, using the last 20 to obtain relevant time and phase averages of the flow and the Nusselt number.

The parallel multi-physics code Alya [39] is used to compute the solution field for the fluid. Alya is based on the Finite Element method and is designed for large-scale parallel applications [40]. vAlya has been extensively validated for many applications. In particular, the present formulation using WALE and ALE has been successfully used to model vortex-induced vibrations in a cylinder [41].

2.2. Appropriateness of the domain and grid sensitivity analysis

The computational grids have been designed by extruding a two-dimensional grid (see Fig. 3) along the x_3 axis for a certain number of planes for a fixed depth of $\widehat{x}_3 = 6$. The coarsest grid considered (for $Re = 50, 100$) has 6,125 nodes per plane with 32 planes, resulting in 196,000 nodes; whereas the finer grids (for $Re = 500, 1,000$) have 44,000 and 50,000 nodes per plane with 50 and 80 planes, resulting in 2.2 and 4.0 million nodes respectively. A mid-size grid (for $Re = 300, 500$) has 15,625 nodes per plane and 40 planes, resulting in 625,000 nodes.

Extensive grid convergence studies have been carried out for each Reynolds numbers considered. As an example, Fig. 4(a-c) shows the grid study for $Re = 500$. The span-wise and time averaged stream-wise velocity profiles at different heights are compared in Fig. 4 (a) showing good agreement between them with minimal differences at the points of maximum and minimum span-wise velocity. A good agreement is also achieved between the centerline time averaged temperatures presented in Fig. 4 (b). Finally, Fig. 4 (c) presents the Nusselt number at the hot wall for the grids considered. Good agreement is observed be-
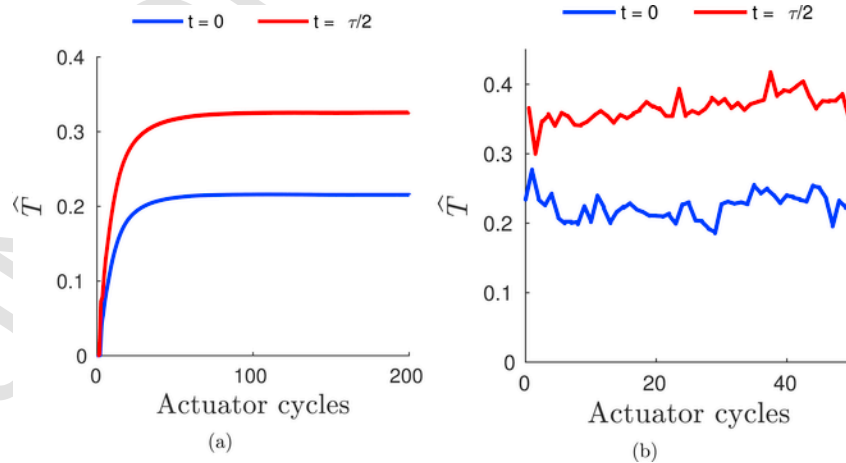
Fig. 2. Time evolution (in actuator cycles) of the temperature at the SJA orifice at $Re = 500$ for maximum expulsion ($t = 0$) and maximum ingestion ($t = \tau/2$) parts of the cycle. (a) URANS k ω SST and a large time-step; (b) LES starting from URANS solution.
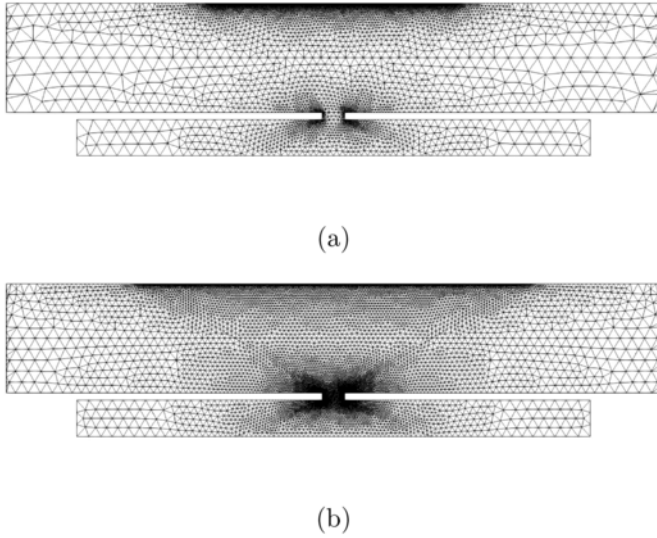
Fig. 3. Computational grid detail, only shown from $\hat{x}_1 = -15$ to $\hat{x}_1 = 15$ and one plane for clarity. (a) Coarse grid: 196,000 nodes with 32 planes. (b) Mid-size grid: 625,000 nodes with 40 planes.
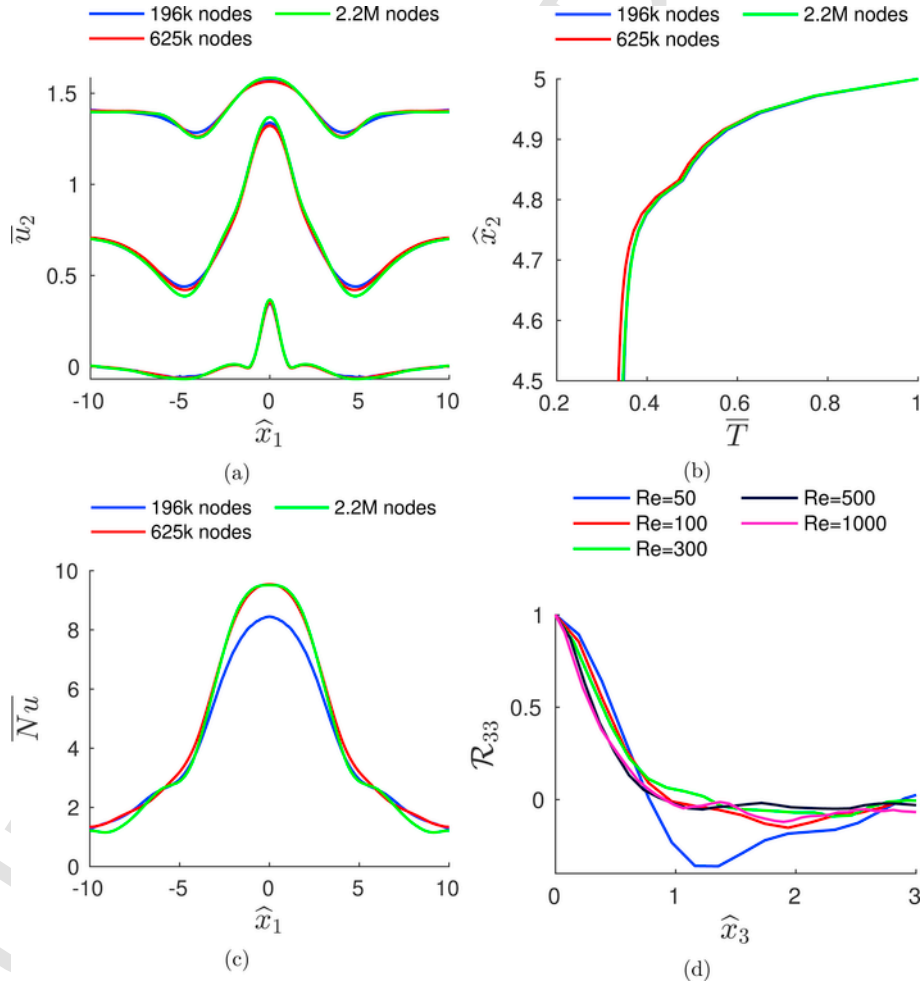
tween the mid-size and fine grids compared with the coarse grid. In this sense, the mid-size grid presents a good compromise between accurate results and computational time. vRegarding the time step, as aforementioned, in the present code it is evaluated at each time step [36]. As an example, for $Re = 500$ and $Re = 1000$ the number of time-steps per actuator cycle is about 13400 and 25200 respectively.

The computational domain in the span-wise direction has been designed so as to contain the largest scales of the flow. Span-wise two point correlations are used to verify if the assumed size is correct for all Reynolds numbers considered in this work. They are defined as

$$\mathcal{R}_{ii} = \frac{\overline{u'_i\left(x_i, t\right) u'_i\left(x_i + \delta, t\right)}}{\overline{u'_i u'_i}} \tag{15}$$

where $\overline{\cdot}$ denotes a time average and $u'_i = u_i - \bar{u}_i$. The values for the two point correlation must tend to zero for the turbulent cases as they approach the half-size of the domain. Fig. 4 (d) presents the span-wise two point correlations for $u_3 u_3$ at $\hat{x}_1 = 0$ and $\hat{x}_2 = 2.5$ for all the Reynolds considered in this study. This position has been selected as a representative point where the jet scales have been fully developed. As seen in the figure, all correlations approach zero at the domain half size, confirming that a domain width of $D/d = 6$ is enough as to contain the largest and more energetic scales, except for $Re = 50$. This could indicate the presence of quasi-laminar structures and a larger do-

Fig. 4. (a) Span-wise and time averaged stream-wise velocity at different heights ($\hat{x}_2 = 0.5$, $\hat{x}_2 = 2.5$ and $\hat{x}_2 = 4.5$, each shifted 0.7 units upwards) for $Re = 500$. (b) Span-wise and time averaged temperature at the jet centerline ($\hat{x}_1 = 0.0$) for $Re = 500$. (c) Span-wise and time averaged Nusselt number at the hot wall ($\hat{x}_2 = 5.0$) for $Re = 500$. (d) Two point correlation for $u_3 u_3$ and different Reynolds numbers, using the finest grid, at $\hat{x}_1 = 0$, $\hat{x}_2 = 2.5$.

main would be needed. However, $D/d = 6$ has been maintained for $Re = 50$ as a good compromise of computational time.

3. Results discussion

The flow on a synthetic jet is very complex. Vortices roll up from the actuator lips and move upwards, where they start to lose coherence and undergo transition to turbulence. Full coalescence is not achieved before the vortices impinge into a hot wall at $\hat{x}_2 = H/d$, and there is a heat exchange between the fluid and the hot wall.

3.1. Instantaneous flow

Typical instantaneous vortical structures of the SJA flow for $Re = 1000$ are shown in Fig. 5. The vortical structures have been identified by means of Q-isocontours [42] where Q is the second invariant of the velocity gradient tensor and is defined as

$$Q = -\frac{1}{2}\frac{\partial u_i}{\partial x_j}\frac{\partial u_j}{\partial x_i} \qquad (16)$$

The condition $Q > 0$ has been found to be effective in identifying regions of coherent vorticity [11,12]. As expected, these regions become more apparent and smaller with the Reynolds number. Four different instants (or phases) can be appreciated: Fig. 5 (a) and (c) are the maximum expulsion ($t = 0$) and maximum ingestion ($t = /2$) phases, while Fig. 5 (b) and (d) are the maximum positive ($t = /4$) and negative ($t = 3/4$) membrane displacement phases.

A large amount of vortical structures can be observed, mostly concentrated in the zones near the neck, both outside and inside the synthetic jet actuator cavity. During the ejection stroke, cold fluid is expelled from the actuator orifice and reaches the top wall at about $t = /4$ (Fig. 5 (b)). Then, the heated fluid is taken inside the actuator during the suction stroke, where it is cooled ($t = 3/4$) before being ejected again (Fig. 5 (d)).

The instantaneous dimensionless temperature at the SJA outlet is shown in Fig. 6 for all Reynolds numbers. The outlet temperature is quite hot, with about $\hat{T} \approx 0.1$ for $Re = 50, 100$ and about $\hat{T} \approx 0.2$ for $Re > 100$. Moreover, the peak to peak temperature variation is large for all Reynolds numbers studied, although the amplitude of the fluctuations decreases with Reynolds due to the enhanced mixing in both

cavities. In the present configuration, the fluid cannot be cooled completely inside the cavity, even assuming that the whole cavity boundaries are at T_∞. vThis results in a decrease of the cooling efficiency of the jet, as seen by Vukasinovic and Glezer [24]. However, as previously seen, this effect stabilizes with time and a stationary state can be reached.

Due to the temporal scales associated with the low velocity zones (see also Section 2.1), it is interesting to identify the frequencies related to these zones as they have an impact on the averaged flow statistics. To do this, a set of numerical probes have been located at different zones of the domain and the signal of the independent variables has been recorded during the whole simulation. These numerical probes are located in the following matrix: $\hat{x}_1 = 0, 5,$ and $10, \hat{x}_2 = 0, 2.5,$ and 4.5 and for each plane in the $\hat{x}_3$ direction.

The signal of different probes at $Re = 500$ located at the same vertical distance from the bottom wall $\hat{x}_2 = 2.5$ but at different $\hat{x}_1$ distance from the jet centerline are plotted in Fig. 7. The energy spectrum of these signals is plotted in Fig. 8. As can be seen from the figures, the signal of probe located in the centerline of the jet is dominated by the periodicity of the ejection and suction events. Notice also the amplitude in the fluctuations of both velocity and temperature, which are the largest of three set of probes. As the flow moves away from the jet centerline, the footprint of the cyclic ejection/suction event can still be observed but also a low frequency modulation in the signal. This is more evident if the signal of the temperature is inspected.

This behavior can be better detected in the spectrum of fluctuations of these signals (see Fig. 8). The SJA main frequency can be seen at all numerical probes, marked in the figures as driving frequency. Yet the energy contained in this peak decreases as the signal of the flow is recorded away from the jet centerline. Notice that both velocity and temperature fluctuations spectra also contain harmonics of the main peak, at frequencies $2f/f_0$ and $3f/f_0$. This is especially evident in the signal registered in the jet centerline. However if the spectrum of the probes located off the jet centerline is analyzed, a broadband low-frequency signal, also marked in the figures, can be seen corresponding to the slow motion of the largest scales of the flow. This peak is centered around $f = 0.0075$ for $Re = 500$, which roughly corresponds with about 7 actuator cycles. These frequencies are also related with the vibration frequencies of the larger structures that have been identified in the flow, as it will be later seen. Moreover, as a result of this low-frequency motion, well-converged statistics of the flow far from the jet
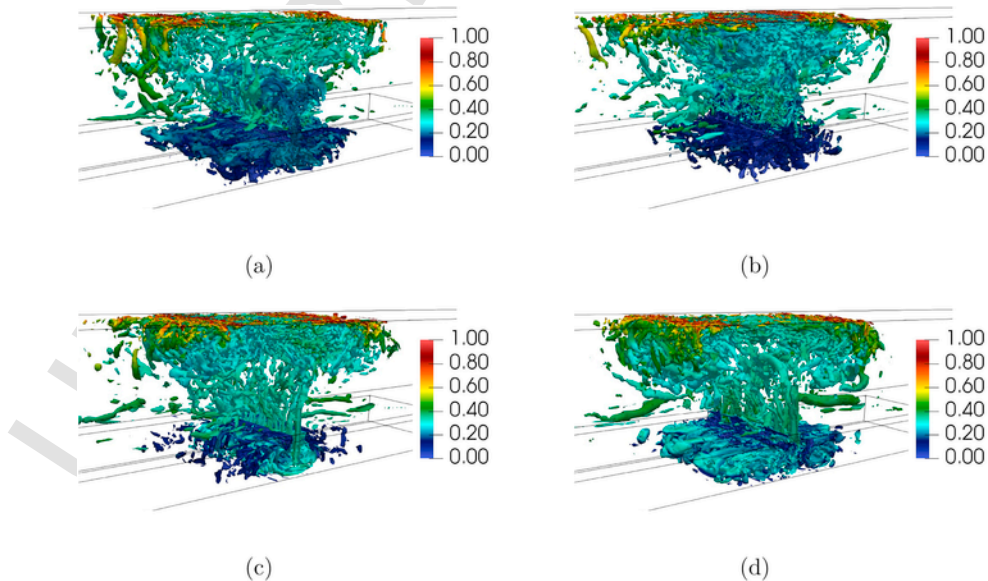

(a)

(b)

(c)

(d)

Fig. 5. Q-isocontours ($Q = 1$) colored by the dimensionless temperature at different phase instants for $Re = 1000$. (a) phase $t = 0$; (b) $t = /4$; (c) $t = /2$; (d) $t = 3/4$.
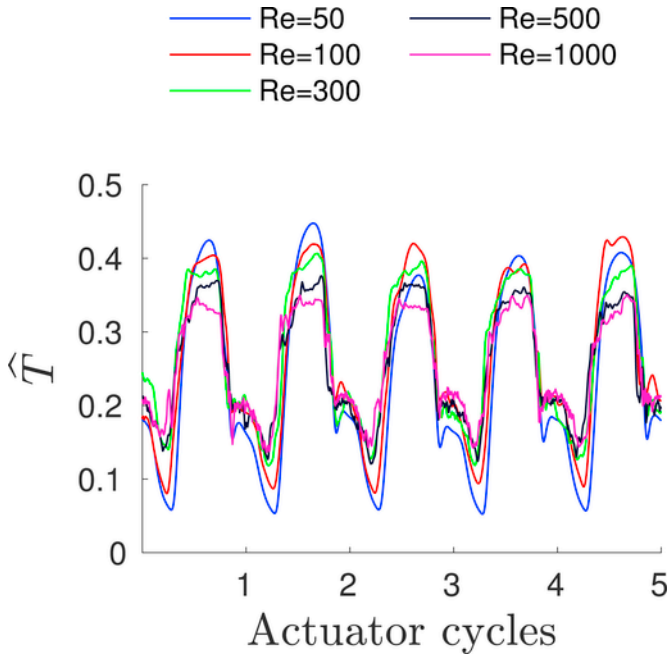
Fig. 6. Time evolution of the span-wise averaged temperature in the SJA neck.

centerline require a longer time integration of at least a few slow-motion full cycles.

3.2. Time and phase averaged flow

Time and phase averaged magnitudes are computed by averaging the last 20 actuator cycles in order to obtain time-accurate statistics (see Section 3.1). Four major vortices (ω_1 to ω_4) have been identified in the time averaged flow, displayed in Fig. 9 for $Re = 500$, selected as representative of all the Reynolds numbers studied.

The result of the coalescence of the vortices ejected from the actuator lips that impinge into the wall is a large clock-wise rotating vortex, ω_1. A second vortex, ω_2, already reported by Ref. [24], is characteristic of the enclosed configuration and is not present in the open configurations, e.g., of Silva-Llanca [11]. These two major vortices, ω_1 and ω_2, dominate the external flow field. They have been identified as regions where $Q > 0$ (shadowed grey areas in Fig. 9) and the positions of their centers, identified by the point where there is a local maximum of Q, have been plotted in Fig. 10 (a), where an increase on the x_1 direction with the Reynolds number can be seen. This fact is also seen in the jet half-width or wake, defined as the distance from the centerline where the velocity deficit has decayed to one-half of its maximum value, represented in Fig. 10 (b), which widens with the Reynolds number. Regarding the latter, it can be seen that for $Re \geq 300$ the jet width is similar, which could be indicative of the turbulent flow being fully developed.

The dynamics of the flow can be appreciated from the phase and span-wise averaged flow in Fig. 11. During the ejection (Fig. 11 (a), $t = 0$), a vortex is expelled from the SJA outlet. This vortex is denoted as ω_1 following the convention set by Silva-Llanca [11]. It eventually merges with the vortex expelled in the previous cycle (ω_0) at the moment of the impingement (Fig. 11 (b), $t = \pi/4$). At this point and when the suction stroke begins (Fig. 11 (c), $t = \pi/2$), an additional vortical structure (ω_s) is created near the impingement point. It sweeps the surface from left to right until it is dissipated. Moreover, ω_s is identified as the main heat transfer enhancement mechanism for jets in the near wall region, which is consistent with the results published in Refs. [11,13,22,43]. The counter clock-wise ω_2 vortex, that is created and destroyed twice per cycle (Fig. 11 (c) and (d)), is also particular of the enclosed configuration. It merges with ω_s while the latter is sweeping the heated wall and this has implications in the heat transfer mechanism, as it will be further discussed.

The flow inside the SJA cavity is also complex and similar to the external flow. Two major structures (see Fig. 9), ω_3 and ω_4, appear as a result of the flow being ingested back into the cavity. The coherent
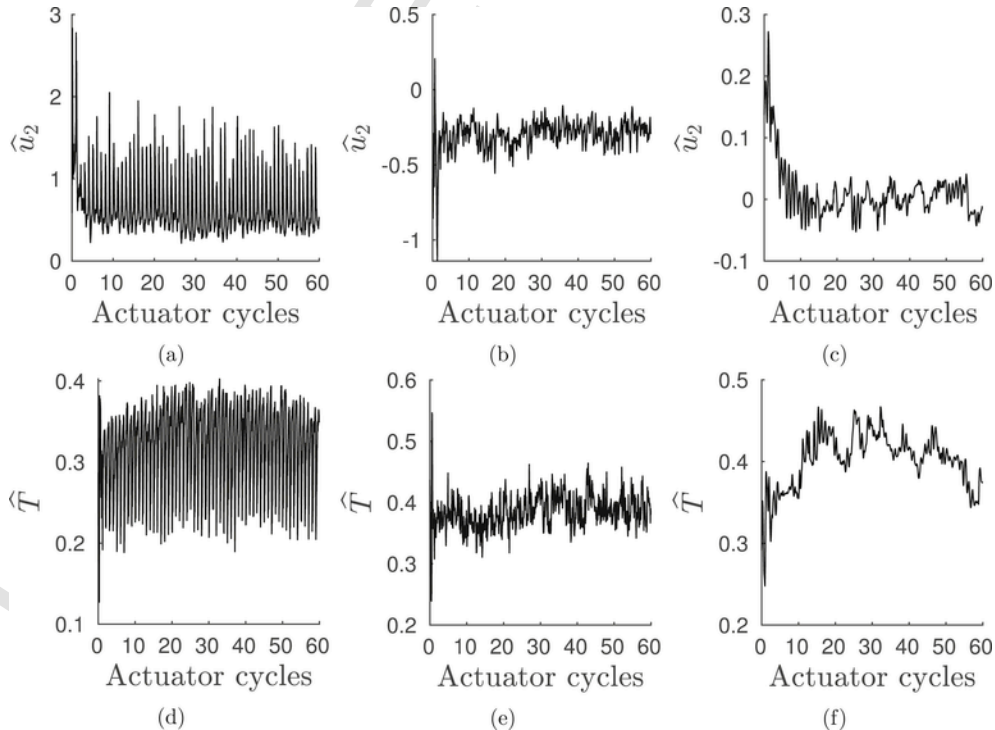

Fig. 7. Temporal evolution of different probes at $Re = 500$ for the span-wise averaged stream-wise velocity (a,b,c) and the span-wise averaged temperature (d,e,f). Probe locations are: (a,d) $\hat{x}_1 = 0$, $\hat{x}_2 = 2.5$; (b,e) $\hat{x}_1 = 5$, $\hat{x}_2 = 2.5$; (c,f) $\hat{x}_1 = 10$, $\hat{x}_2 = 2.5$.
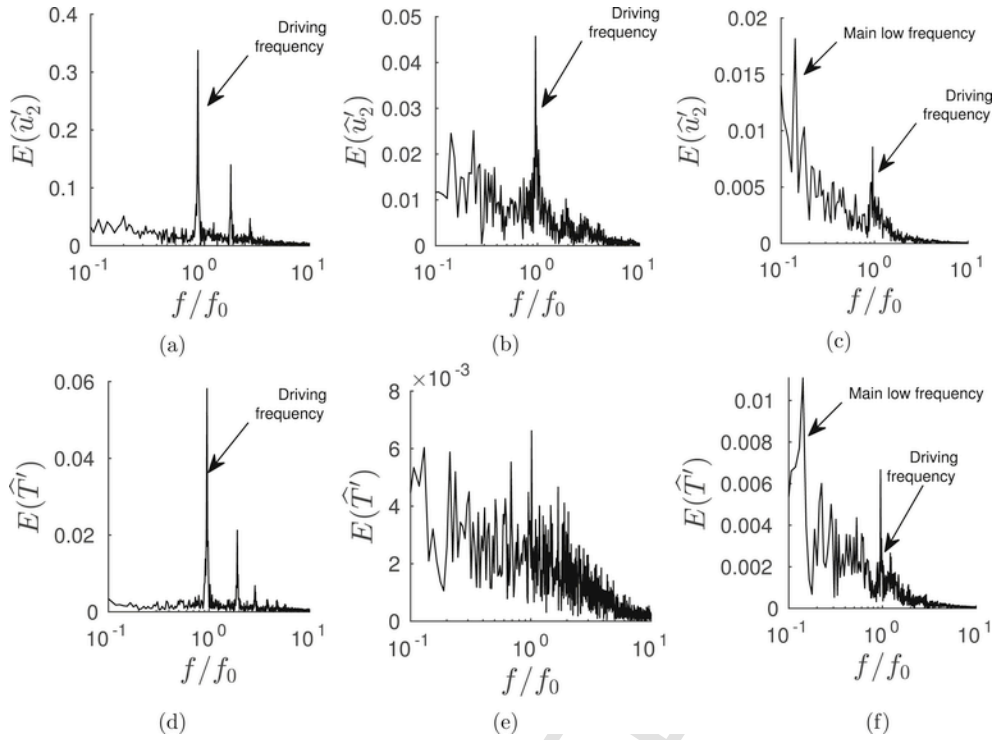
Fig. 8. Energy spectrum of different probes at $Re = 500$ for the span-wise averaged stream-wise velocity (a,b,c) and the span-wise averaged temperature (d,e,f). Probe locations are: (a,d) $\hat{x}_1 = 0$, $\hat{x}_2 = 2.5$; (b,e) $\hat{x}_1 = 5$, $\hat{x}_2 = 2.5$; (c,f) $\hat{x}_1 = 10$, $\hat{x}_2 = 2.5$.
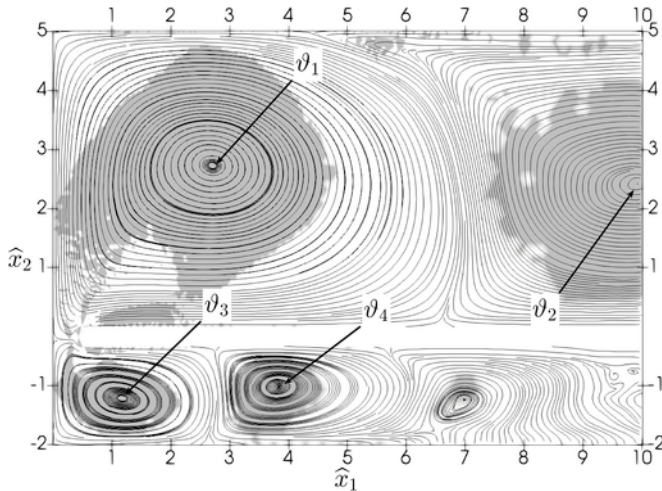

Fig. 9. Time and span-wise averaged velocity streamlines for $Re = 500$ with the regions with $Q > 0$ highlighted in the background (right-hand half of the computational domain).

structure ϑ_4 is the analogous of ϑ_2 but inside the cavity. Regarding the flow dynamics, a vortex, ϑ_3, rolls down from the actuator lips and impinges into the actuator membrane (Fig. 11 (c), $t = \pi/2$), where heat transfer occurs. Eventually another coherent structure, ϑ_4, appears due to the aforementioned process (Fig. 11 (d), $t = 3\pi/4$).

The conditions at the SJA outlet (both for the flow field and the temperature) are important in order to understand the jet dynamics. In this line, span-wise and phase averaged stream-wise velocity and temperature profiles at the SJA neck are shown in Fig. 12. Although there is a similarity when comparing the stream-wise velocity profiles (due to having considered the same JFC), the flow is not symmetrical between the ejection and suction strokes. During the first one ($t = 0$), the stream-wise velocity shows a sinusoidal profile due to the effect of the

SJA neck, while in the latter ($t = \pi/2$) the profile is nearly plug-like. Moreover, during the transition between ejection and suction ($t = \pi/4$ and $t = 3\pi/4$), the flow is reversed at the vicinity of the wall, having implications for the development of models for the flow at the SJA outlet. This behavior is in line to what Kotapati et al. [9] observed when modeling the SJA cavity. Regarding the temperature field, a notable difference of temperature between ejection and suction parts of the cycle is again observed. In addition, the temperature field becomes more uniform with the Reynolds number, due to the increase in turbulent mixing. This fact strongly supports the validity of an uniform model for the outlet temperature profile for turbulent Reynolds numbers $Re > 100$.

An expression for the temperature at the SJA outlet with the Reynolds number can be obtained from space averaging the data in Fig. 12. The correlation, shown in Figure Fig. 13, is

$$\langle \hat{T} \rangle = aRe^b \tag{17}$$

where the coefficients are $a = 0.075$ and $b = 0.137$.

The agreement is fair for all Reynolds numbers (relative error below 6%) although the result from the correlation is more representative of the flow at $Re > 100$ as the temperature at the outlet presents a flatter profile at larger Reynolds numbers. This data can be used to generate a boundary condition for the temperature at the SJA outlet for JFC = 3 vand a $H/d = 5$. Hoewever, for other H/d ratios or actuator geometries the outlet temperatures could differ significantly.

3.3. Heat transfer analysis

The instantaneous local Nusselt number at the hot wall is defined as

$$Nu = \frac{\partial \hat{T}}{\partial \hat{x}_2}\bigg|_{\hat{x}_2 = H/d} \tag{18}$$

and is shown in Fig. 14 for various phase instants at $Re = 50$, $Re = 500$ and $Re = 1000$. The thermal footprint can be clearly seen on
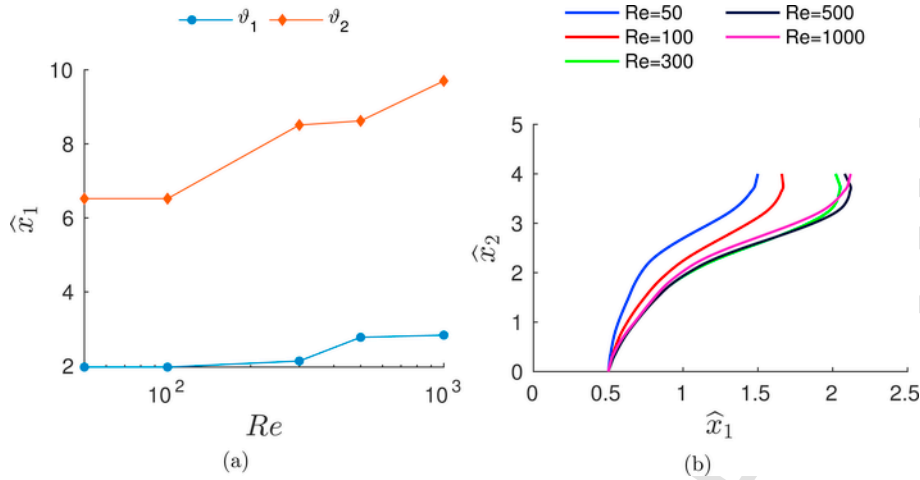
Fig. 10. (a) Coordinates of the vortex centers for different Re. (b) Jet half-width with the domain height for various Reynolds numbers.
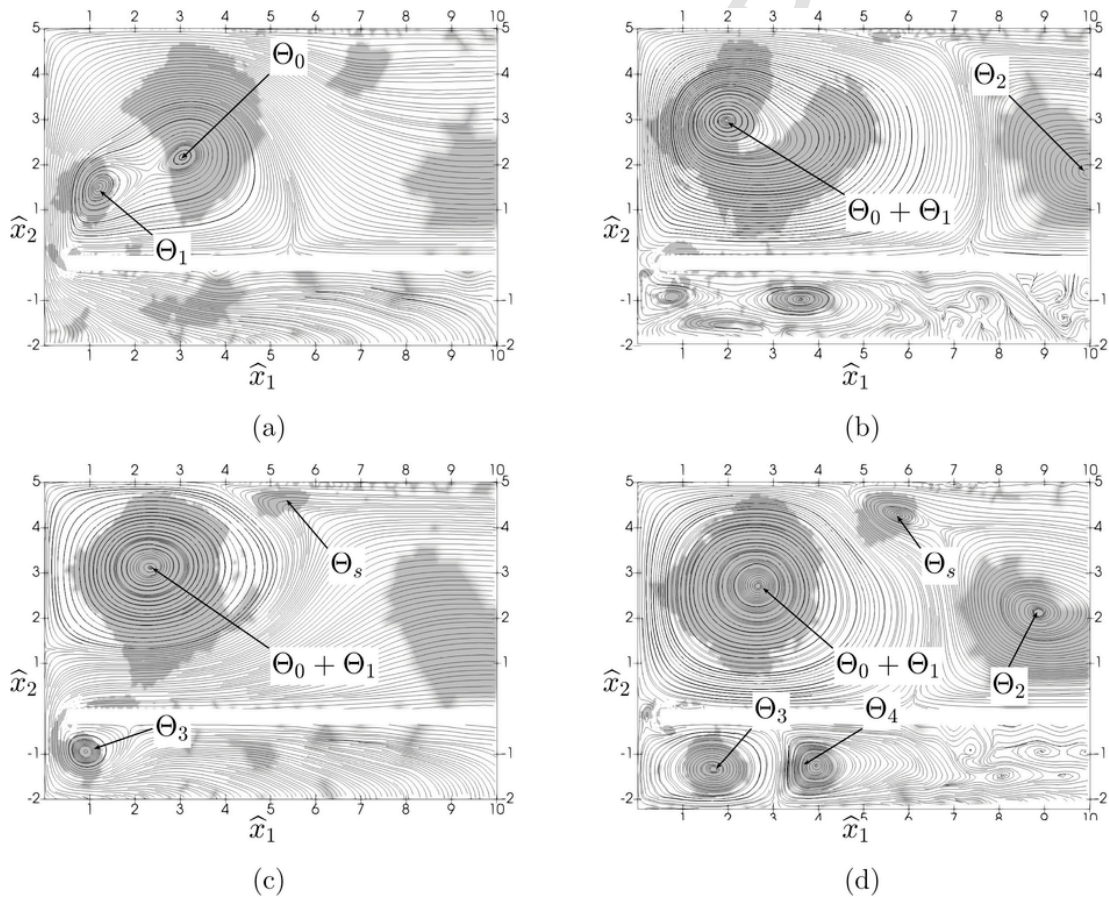

Fig. 11. Phase and span-wise averaged velocity streamlines for $Re = 500$ with the regions with $Q > 0$ highlighted in the background (right-hand half of the computational domain). (a) phase $t = 0$; (b) $t = \pi/4$; (c) $t = \pi/2$; (d) $t = 3\pi/4$.

the hot wall, which intensifies with the Reynolds number, as expected. The maximum heat transfer occurs at the moment of the impingement ($t = \pi/4$) and lasts until the start of the suction cycle at $t = \pi/2$. The high Nusselt number regions spread along the heated wall, reaching more homogeneous values thanks to the effect of ϑ_s sweeping the wall. The footprint of the turbulent (or transitional for the lower Reynolds number) large-scale elongated vortices can also be seen in the image as regions of high and low heat transfer coefficient following the vortex patterns. The spanwise size of these vortices decreases as the Reynolds number increases. However, the footprint of these structures is lost

when averaging the signal and the span-wise and time averaged Nusselt distribution is symmetric.

The time and span-wise averaged local Nusselt number ($\overline{Nu}_{avg}$) is shown in Fig. 15. It is presented for each Reynolds number considered, as well as the results from Ref. [18] at $Re = 508$, $Sk = 12.7$ (equivale to JFC = 3.15) for an open configuration. As can be seen, for $Re = 500$, near the stagnation point the agreement with the experimental results is quite good, despite the difference in the configuration and JFC. However, the Nusselt number decays significantly faster than in the open configuration for distances roughly larger than the jet
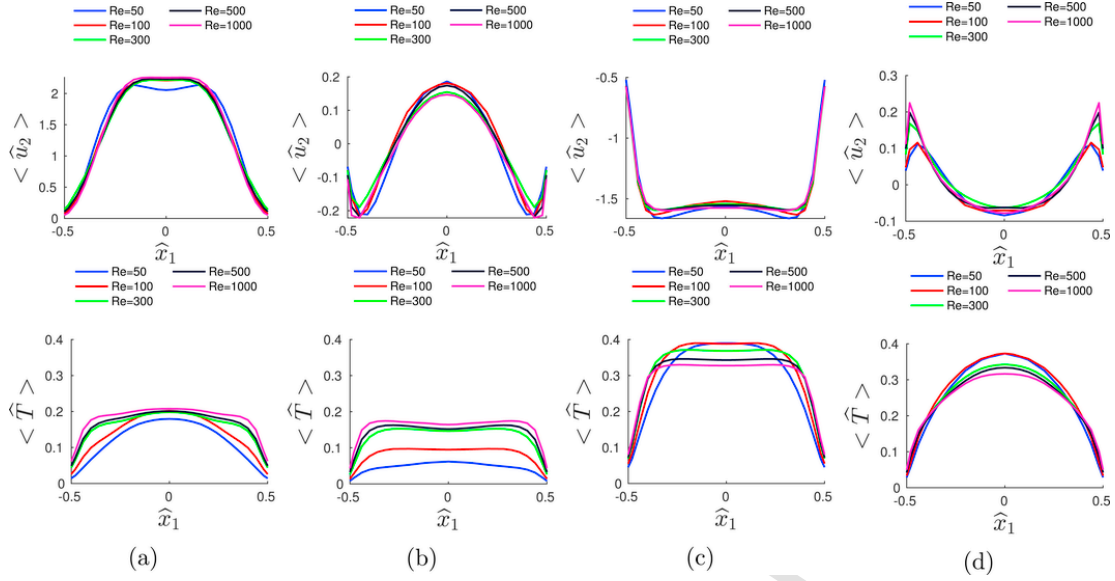
Fig. 12. Phase and span-wise averaged velocity and temperature profiles at the actuator lips for all the Reynolds studied. (a) phase $t = 0$; (b) $t = \pi/4$; (c) $t = \pi/2$; (d) $t = 3\pi/4$.
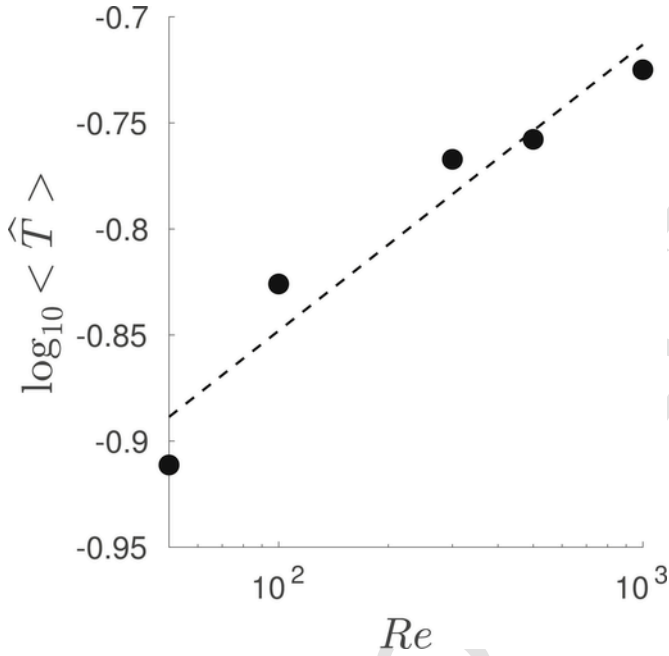

Fig. 13. Phase and space-averaged SJA outlet temperature during suction for different Reynolds numbers. The dashed line correspond to the correlation in Eq. (17).

wake. This is due to the aforementioned effect of ω_s merging into ω_2. While in the open configuration ω_s can freely sweep the heated wall and produce a heat transfer enhancement effect, in the confined configuration this is prevented by ω_2.

The time and space averaged overall Nusselt number ($\overline{Nu}_{avg}$), integrated between $\hat{x}_1 = \pm 5$, for different Reynolds numbers is shown in Fig. 16. A correlation is proposed following the work in Ref. [21].

$$\frac{\overline{Nu}_{avg}}{Pr^{0.42}} = aRe^m \tag{19}$$

where $a = 0.115$ and $m = 0.682$. As a means of comparison, the experimental points for the open configuration tested in Ref. [18] at JFC = 3.15 are plotted in Fig. 16. Note that in the figure only the experimental data for $H/d = 5$ is included. For the lower Reynolds num-

bers, the configuration here studied yields lower values for the Nusselt number than for the open cavity but even though the flow configuration is different, in terms of the average Nusselt number both configurations yield quite close results, specially within the zone $\hat{x}_1 = \pm 5$ where the behavior of the local Nusselt number is similar, as observed in Fig. 15.

4. Conclusions

A synthetic jet enclosed between two large parallel plates and impinging into a hot plate has been studied for $Re = 50; 100; 300; 500; 1,000$ and JFC = 3. For the lower Reynolds numbers DNS of the flow have been performed, whereas for $Re > 100$, LES using the WALE SGS model have been carried out. The proposed formulation accounts for the time-periodic movement of the SJA membrane using an ALE method, therefore, the actuator frequency f_0 and velocity U_0 are coupled and the jet formation criteria becomes a geometrical parameter. A simplified rectangular actuator in an homogeneous domain in the x_3 direction has been studied with a orifice to cavity height of $H/d = 5$.

The resulting flows are quite complex, and a large number of actuator cycles has to be integrated in order to reach a statistically stationary state. This study shows that, for the present configuration, the far flow field is dominated by frequencies about 7 times lower than the driving frequency, resulting in the overall system having slow temporal scales. The flow is inherently three dimensional, even for the lowest Reynolds numbers considered, which has an effect on the Nusselt number and the size of the vortices. The external flow in the enclosed configuration is dominated by two major structures, ω_1 and ω_2, that have a counterpart inside the actuator, ω_3 and ω_4. The largest of them, (i.e., ω_1), has been identified in both open and enclosed configurations and is the result of the coalescence of the vortices expelled by the actuator. However, the second structure (i.e., ω_2), is specific of the enclosed configuration and appears as a result of the flow interacting with the bottom wall. It plays a major role in limiting the jet's heat transfer enhancement mechanism, which results in a higher decay of the Nusselt number far from the stagnation point when compared with the open configuration. It has been determined that, as an average, the outlet jet temperature is 1/5 of the temperature difference between the hot and bottom plates. Thus, the imposition of an outlet temperature equal to
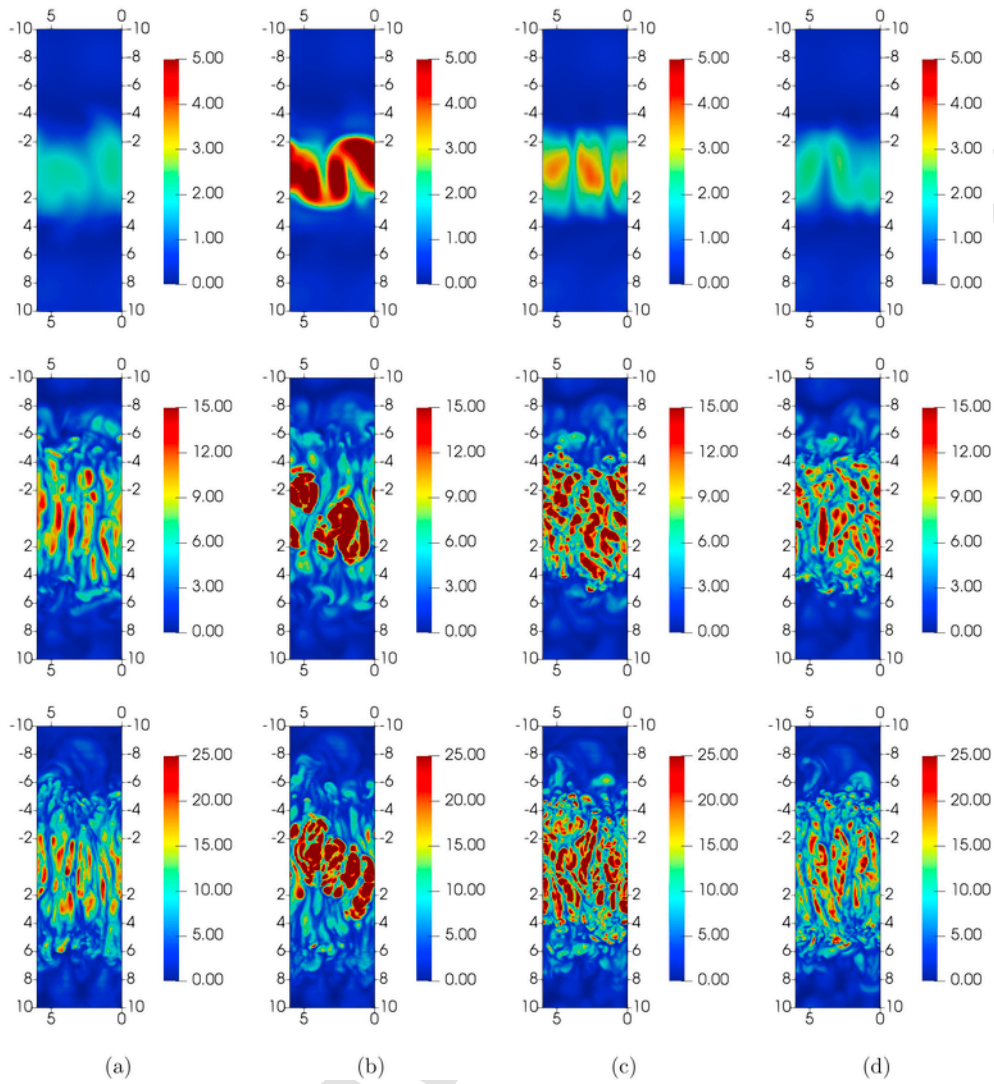
Fig. 14. Instantaneous local Nusselt number at the hot wall for $Re = 50$ (top), $Re = 500$ (mid) and $Re = 1000$ (bottom). Phases: (a) $t = 0$; (b) $t = \pi/4$; (c) $t = \pi/2$; (d) $t = 3\pi/4$.
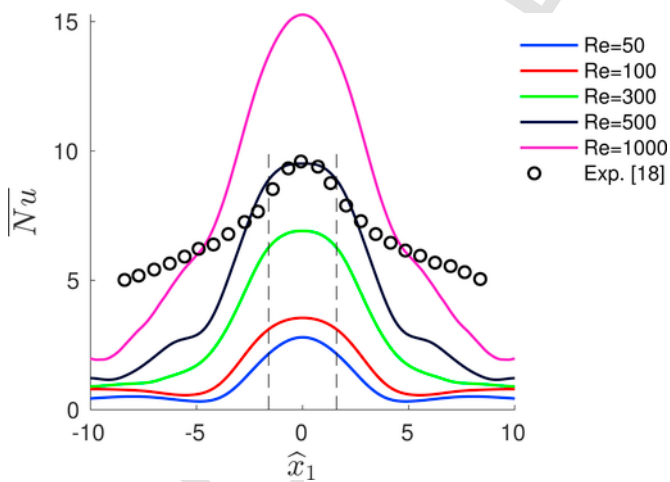

Fig. 15. Time and span-wise averaged Nusselt number for various Reynolds number. The dashed line corresponds to the jet wake half-width for $Re = 500$. The black circles are the experimental results from Ref. [18] (open configuration) at $Re = 508$, $Sk = 12.7$.
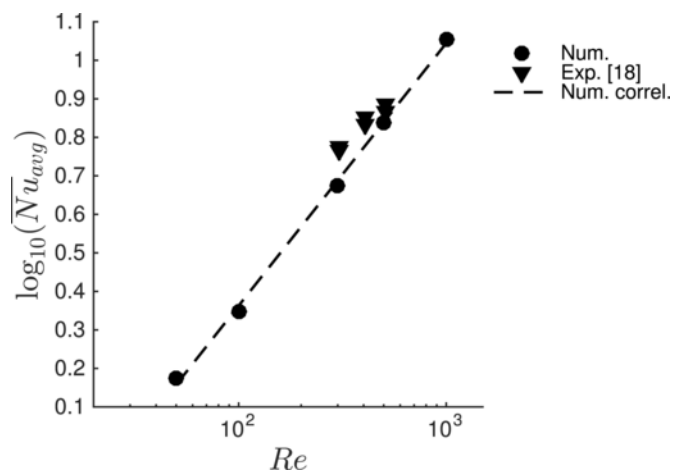

Fig. 16. Nusselt number correlation with Reynolds number. The dashed line corresponds to the correlation presented in Eq. (19). The triangles correspond to the experimental points presented in Ref. [18] for an open configuration at $Sk = 12.7$ (JFC = 3.15).

the cold temperature in numerical simulations might result in an overestimation of the Nusselt number in the hot wall.

In addition, the model proposed allows to compute accurate velocity and temperature profiles at the actuator neck, values that are generally unknown when considering other SJA models, and that have an impact on the heat transfer. The analysis of the conditions at the outlet has shown that: (i) the outlet temperature is about 1/10 to 1/5 of the temperature difference between the hot and cold plates depending on the Reynolds number; (ii) there is a similarity between the different Reynolds numbers considered at the same JFC; (iii) a strong asymmetry appears in the flow between ejection and suction phases; (iv) uniform-like temperature outlet profiles have been obtained for $Re > 100$, thus supporting the validity of a uniform outlet temperature model. Correlations of outlet temperature and Nusselt number have been obtained for the enclosed configuration. The former can be used as a model for the outlet jet temperature in the present configuration.

Acknowledgements

References

[1] Ari Glezer, Michael Amitay, Synthetic jets, Annu. Rev. Fluid Mech. 34 (2002) 503 529.
[2] L. Kral, J. Donovan, A. Cain, A. Cary, Numerical simulation of synthetic jet actuators, In: 4th Shear Flow Control Conference, vols. 97 1824, 1997, p. 15.
[3] S. Mallinson, G. Hong, J. Reizes, Some characteristics of synthetic jets, In: 30th Fluid Dynamics Conference, vol. 3651, 1999, p. 10.
[4] S.G. Mallinson, C.Y. Kwok, J.A. Reizes, Numerical simulation of micro-fabricated zero mass-flux jet actuators, Sens. Actuators, A 105 (2003) 229 236.
[5] C.L. Rumsey, T.B. Gatski, W.L. Sellers III, V.N. Vatsa, S.A. Viken, Summary of the 2004 computational fluid dynamics validation Workshop on synthetic jets, AIAA J. 44 (2006) 194 207.
[6] B.L. Smith, A. Glezer, The formation and evolution of synthetic jets, Phys. Fluids 10 (1998) 2281 2297.
[7] Y. Utturkar, R. Holman, R. Mittal, B. Carroll, M. Sheplak, L. Cattafesta, A jet formation criterion for synthetic jet actuators, In: 41st Aerospace Sciences Meeting and Exhibit, 2003, pp. 1 9.
[8] R. Holman, Y. Utturkar, R. Mittal, B.L. Smith, L.N. Cattafesta, Formation criterion for synthetic jets, AIAA J. 43 (2005) 2110 2116.
[9] R.B. Kotapati, R. Mittal, L.N. Cattafesta, Numerical study of a transitional synthetic jet in quiescent external flow, J. Fluid Mech. 581 (2007) 287.
[10] C. Yao, F.J. Chen, D. Neuhart, Synthetic jet flowfield database for computational fluid dynamics validation, AIAA J. 44 (2006) 3153 3157.
[11] L. Silva-Llanca, A. Ortega, Vortex dynamics and mechanisms of heat transfer enhancement in synthetic jet impingement, Int. J. Therm. Sci. 112 (2017) 153 164.
[12] J.C.R. Hunt, A.A. Wray, P. Moin, Eddies, streams, and convergence zones in turbulent flows, In: Proceedings of the Summer Program 1988, 1989.
[13] A. Pavlova, M. Amitay, Electronic cooling using synthetic jet impingement, J. Heat Tran. 128 (2006) 897 907.
[14] L.D. Mangate, Mangesh B. Chaudhari, Heat transfer and acoustic study of impinging synthetic jet using diamond and oval shape orifice, Int. J. Therm. Sci. 89 (2015) 100 109.
[15] G. Eschmann, A. Kuntze, W. Uffrecht, E. Kaiser, S. Odenbach, Experimental and numerical investigation of heat transfer coefficients in gaseous impinging jets. First test of a recent sensor concept for steady and unsteady flow, Int. J. Therm. Sci. 96 (2015) 290 304.
[16] M.A. Pakhomov, V.I. Terekhov, RANS modeling of flow structure and turbulent heat transfer in pulsed gas-droplet mist jet impingement, Int. J. Therm. Sci. 100 (2016) 284 297.
[17] T. Guan, J.Z. Zhang, Y. Shan, Convective heat transfer by a row of tab-excited impinging jets on a wedge-shaped concave surface, Int. J. Therm. Sci. 100 (2016) 37 53.
[18] L. Silva-Llanca, A. Ortega, I. Rose, Experimental convective heat transfer in a geometrically large two-dimensional impinging synthetic jet, Int. J. Therm. Sci. 90 (2015) 339 350.
[19] O. Ghaffari, S.A. Solovitz, M. Arik, An investigation into flow and heat transfer for a slot impinging synthetic jet, Int. J. Heat Mass Tran. 100 (2016) 634 645.
[20] O. Ghaffari, S.A. Solovitz, M. Ikhlaq, M. Arik, An investigation into flow and heat transfer of an ultrasonic micro-blower device for electronics cooling applications, Appl. Therm. Eng. 106 (2016) 881 889.
[21] L. Silva-Llanca, A. Ortega, Convective heat transfer in an impinging synthetic jet: a numerical investigation of a canonical geometry, J. Heat Tran. 135 (7 9) (2013).
[22] Y. Utturkar, M. Arik, C.E. Seeley, M. Gursoy, An experimental and computational heat transfer study of pulsating jets, J. Heat Tran. 130 (1 10) (2008).
[23] K. Habibi, S. Amiri, M. Ashjaee, Study of mixed convection characteristics of confined planar jet impingement using the direct temperature gradient interferometric method, Int. J. Therm. Sci. 71 (2013) 205 215.
[24] J. Vukasinovic, A. Glezer, Spot-cooling by confined, impinging synthetic jet, Heat Tran. 3 (2003) 469 476.
[25] M. Hatami, F. Bazdidi-Tehrani, A. Abouata, A. Mohammadi-Ahmar, Investigation of geometry and dimensionless parameters effects on the flow field and heat transfer of impingement synthetic jets, Int. J. Therm. Sci. 127 (2018) 41 52.
[26] Hao Xia, Ning Qin, Dynamic grid and unsteady boundary conditions for synthetic jets flow, In: 43rd AIAA Aerospace Sciences Meeting and Exhibit, 2005, pp. 1 9.
[27] D.P. Rizzetta, M.R. Visbal, M.J. Stanek, Numerical investigation of synthetic-jet flowfields, AIAA J. 37 (8) (1999) 919 927.
[28] C.Y. Lee, D.B. Goldstein, Two dimensional synthetic jet simulation, AIAA J. 40 (3) (2002) 510 516.
[29] E. Montazer, M. Mirzaei, E. Salami, T.A. Ward, F.I. Romli, S.N. Kazi, Optimization of a synthetic jet actuator for flow control around an airfoil, IOP Conf. Ser. Mater. Sci. Eng. 152 (1) (2016) 012023.
[30] Y.H. Liu, S.Y. Tsai, C.C. Wang, Effect of driven frequency on flow and heat transfer of an impinging synthetic air jet, Appl. Therm. Eng. 75 (2015) 289 297.
[31] Q. Gallas, On the Modeling and Design of Zero-net Mass Flux Actuators, PhD thesis University of Florida, 2005.
[32] M.A. Feero, P. Lavoie, P.E. Sullivan, Influence of cavity shape on synthetic jet performance, Sensor Actuator Phys. 223 (1 10) (2015).
[33] F. Nicoud, F. Ducros, Subgrid-scale stress modelling based on the square of the velocity gradient tensor, Flow, Turbul. Combust. 62 (1999) 183 200.
[34] D. Mira, X. Jiang, C. Moulinec, D.R. Emerson, Numerical investigation of the effects of fuel variability on the dynamics of syngas impinging jet flames, Fuel 103 (2013) 646 662.
[35] F. Capuano, G. Coppola, L. Rández, L. De Luca, Explicit Runge Kutta schemes for incompressible flow with improved energy-conservation properties, J. Comput. Phys. 328 (2017) 86 94.
[36] F.X. Trias, O. Lehmkuhl, A self-adaptive strategy for the time integration of Navier-Stokes equations, Numer. Heat Tran., Part B: Fundamentals 60 (2) (2011) 116 134.
[37] A. Masud, Effects of mesh motion on the stability and convergence of ALE based formulations for moving boundary flows, Comput. Mech. 38 (2006) 430 439.
[38] F.R. Menter, Two-equation eddy-viscosity turbulence models for engineering applications, AIAA J. 32 (1994) 1598 1605.
[39] BSC-CNS, Alya multiphysics code, in: http://www.bsc.es/computer-applications/alya-system, 2014.
[40] M. Vázquez, G. Houzeaux, S. Koric, A. Artigues, J. Aguado-Sierra, R. Arís, D. Mira, H. Calmet, F. Cucchietti, H. Owen, et al., Alya: multiphysics engineering simulation toward exascale, Journal of Computational Science 14 (15 27) (2016).
[41] D. Pastrana, J.C. Cajas, O. Lehmkuhl, I. Rodríguez, G. Houzeaux, Large-eddy simulations of the vortex-induced vibration of a low mass ratio two-degree-of-freedom circular cylinder at subcritical Reynolds numbers, Comput. Fluids 0 (1 15) (2018).
[42] J. Jeong, F. Hussain, On the identification of a vortex, J. Fluid Mech. 285 (1995) 69 94.
[43] P. Valiorgue, T. Persoons, A. McGuinn, D.B. Murray, Heat transfer mechanisms in an impinging synthetic jet for a small jet-to-surface spacing, Exp. Therm. Fluid Sci. 33 (2009) 597 603.